THE JOURNAL OF PHYSICAL CHEMISTRY C

Article

pubs.acs.org/JPCC

Electronic Properties and Quantum Confinement in Bi_2S_3 Ribbon-Like Nanostructures

V. Calzia,*[,†] G. Malloci,[‡] G. Bongiovanni,[†] and A. Mattoni*[,‡]

[†]Dipartimento di Fisica, Università di Cagliari, Cittadella Universitaria, I-09042 Monserrato (Cagliari), Italy

[‡]Istituto Officina dei Materiali (CNR-IOM), Unità di Cagliari, Cittadella Universitaria, I-09042 Monserrato (Cagliari), Italy

ABSTRACT: In this work we study the morphology and electronic properties of Bi_2S_3 nanostructures by means of atomistic simulations. We focus on elongated nanoribbons that are the building blocks of the corresponding crystal structures, and we study saturated and unsaturated nanocrystals of finite size in comparison with one-dimensional infinite ones. By means of (time-dependent) density functional theory calculations we provide evidence that the optical gap can be tuned through quantum confinement with sizable effects for ribbons smaller than three nanometers. By a comparison with Sb_2S_3, we conclude that Bi_2S_3 nanostructures have similar tunability of the bandgap and a better tendency of passivating defects at the (010) surfaces through local reconstructions.

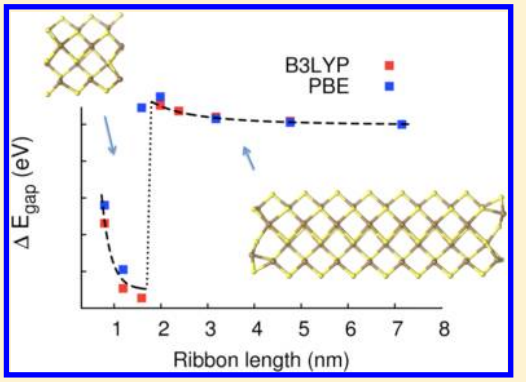

INTRODUCTION

Pnictogen sulfides are a class of compounds that usually exist in nature as minerals. Because of their abundance and cheapness[1] and their interesting physical properties, they have been object of increasing scientific interest. In particular, metal sulfide nanostructures have been employed in several kinds of devices, such as solar cells, light-emitting diodes, sensors, thermoelectric devices, lithium-ion batteries, fuel cells, and nonvolatile memory devices.[2−4] Because of their good light absorption, some metal sulfides, such as stibnite (Sb_2S_3), have been used to sensitize solid-state hybrid solar cells in order to improve the absorption of solar photons and to inject photogenerated electrons into titania (TiO_2). Efficiencies as high as 5% have been achieved in polymer/metaloxide (e.g., P3HT/Sb_2S_3/TiO_2) solar cells.[5] Unfortunately, because of its toxicity, stibnite is not the best option for commercial use. Bismuth sulfide, also called bismuthinite (Bi_2S_3), has been recently recognized as a valid environmental friendly alternative to stibnite.[6] The two sulfides have the same crystallographic symmetry: they both belong to the *Pnma* space group with an orthorhombic unit cell that contains 20 atoms. The crystal structure is strongly anisotropic, consisting in tightly bonded units of Bi_4S_6 (also called ribbons) in an herringbone arrangement (see Figure 1). Each ribbon is a long (infinite, in the perfect crystal) chain of atoms connected by ionic/covalent bonds, which extend along the [010] direction. Interactions between neighbor ribbons are weak[7,8] and due to van der Waals dispersive forces.

Bi_2S_3 is tipically synthesized in nanocrystalline form, with individual grains of the order of tens of nanometers.[9,10] Several techniques have been explored to efficiently synthesize nanocrystalline Bi_2S_3 via colloidal solutions.[9−12] Colloidal synthesis has the advantage of being much cheaper than

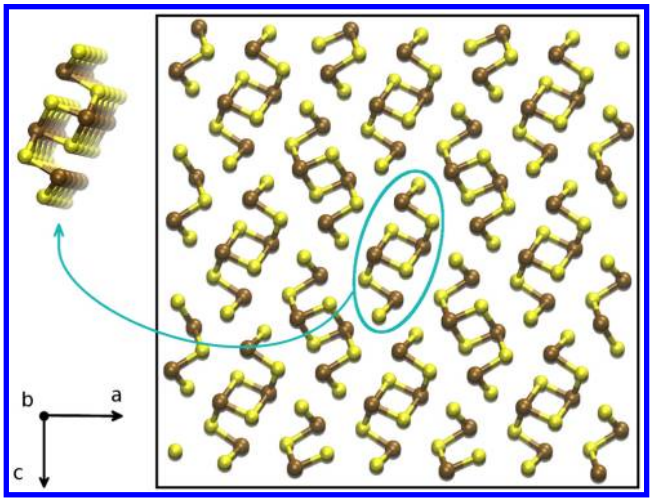

Figure 1. Crystal structure of Bi_2S_3 and Sb_2S_3 (S atoms in yellow; Bi/Sb atoms in brown). The bulk consists in an herringbone pattern of ribbons (see single ribbon in the inset) extending along the [010] direction.

molecular beam epitaxy or other expensive growing methods requiring ultrahigh vacuum conditions. By varying the solvent, the temperature, and the time of growth, it is possible to form nanocrystals of controlled size.[11] These techniques have been already successfully exploited in photovoltaics to produce bulk heterojunctions by blending Bi_2S_3 with PbS nanocrystals[13] or by depositing Bi_2S_3 nanoparticles on nanoporous substrates to

Received: June 10, 2013
Revised: September 18, 2013

   dx.doi.org/10.1021/jp405740b | *J. Phys. Chem. C* XXXX, XXX, XXX−XXX

enhance light absorption and electron injection.[14] For all the reasons explained above (nontoxicity, low-cost synthesis, and good absorption properties) there has been a growing attention to Bi_2S_3 and, together with the experimental investigations, a series of theoretical studies[8,15] was developed to better understand the experimental observations. All the compounds of the stibnite family where recently studied using state-of-the-art first-principles calculations in the context of semiconductor-sensitized solar cells.[16,17] In addition to the bulk properties, the study of nanosize effects on the electronic properties of the nanostructures is of great relevance. In particular it is interesting to understand the structure and the atomic relaxations occurring in nanosized objects and, more importantly, to clarify whether and to what extent it is possible to tune the optical properties by controlling the size of the nanoparticles. At variance with Sb_2S_3 for which this problem has been already addressed,[18] to our knowledge, a systematic study of Bi_2S_3 properties as a function of nanocrystal dimension is missing and it is the object of the present work.

Here, we investigate through *ab initio* methods the electronic and optical properties of Bi_2S_3 and Sb_2S_3 nanostructures and their dependence on the size through quantum confinement effects, studying elongated nanostructures consisting of ribbons of nanometric lengths. Our calculations are consistent with experimental results and provide evidence that the optical gap can be tuned through quantum confinement with sizable effects for ribbons smaller than about three nanometers.

METHODS

For periodic structures (i.e., bulk and infinite ribbons), we performed density functional theory (DFT)[19] calculations by using the QUANTUM ESPRESSO code.[20] The initial geometry was chosen corresponding to the experimental data reported by Lundegaard et al.[7] We used the Perdew–Burke–Ernzerhof (PBE)[21] functional within the generalized gradient approximation (GGA) of DFT to perform geometry optimizations. The valence electron wave functions are expanded in planewaves basis sets with kinetic energy cutoff of 30 Ry. Valence electrons are explicitly described, while the core–valence interaction is taken into account by means of Troullier–Martins pseudopotentials.[22] The reciprocal space was sampled with a $4 \times 4 \times 4$ Brillouin zone mesh centered at Γ. Both the energy cutoff and the number of *k*-points were tested to be sufficient to ensure convergence of the total energy of the system. For single ribbons we sample the reciprocal space with a $1 \times 4 \times 1$ mesh, according to the one-dimensionality of the ribbon.

For the finite size nanocrystals the DFT calculations were performed by using the TURBOMOLE software,[23] which is suitable for nonperiodic systems. We used both the PBE and B3LYP[24] functionals. For the electronic wave functions we used the default single valence polarized (def-SV(P)) basis set of Gaussian-type orbitals in conjunction with an effective core potential including 78 (46) core electrons for Bi (Sb). We proved the accuracy of such a basis set by comparing the results with the computationally heavier triple-ζ valence polarized basis set (def-TZVP). To check the validity of the methodology adopted, we performed test calculations by taking into account the spin–orbit coupling,[25] the inclusion of Bi semicore states,[26] and the quasi-particle correction to the DFT Kohn–Sham gaps as computed through the ΔSCF method.[27]

In principle, DFT is correct only for ground-state properties of the investigated system. Optical excited states are properly described for finite systems by time-dependent DFT (TDDFT).[28] To compute the excitation energies we used the TDDFT implementation of TURBOMOLE based on the linear response of the density-matrix, in which the poles of the linear response function correspond to vertical excitation energies and the pole strengths to the corresponding oscillator strengths.[29] The above computational methodology has been previously applied for zinc-oxide[30] and zinc-sulfide[31] nanocrystals for which we found a general good agreement between DFT/TDDFT results and many-body perturbation theory calculations.[31]

RESULTS

Periodic Structures. We first characterize the properties of the crystalline bulk material starting from available experimental data.[7] Our calculated Bi_2S_3 electronic gap is 1.40 and 1.50 eV in the initial and relaxed structure, respectively. These values are in good agreement with Sharma et al.[32] (1.45 eV with GGA-PBE) and Caracas and Gonze[8] (1.47 eV with the local density approximation). Moreover, consistently with previous theoretical literature, the bandgap of the relaxed crystal is nearly direct.[15] Experimental data are quite scattered and report a bandgap in between 1.2 and 1.7 eV.[33−36] Note that, as recently reported by Filip et al.,[17] the agreement between DFT Kohn–Sham gaps and the experimental results for the crystalline bulk material comes from the fortuitous cancellation between spin–orbit and quasi-particle effects.

Since in the present work we are interested in nanocrystalline materials we need to identify models of nanoparticles. In particular we focus on single ribbons that are the building blocks of the crystal structure, and we calculate the properties of an isolated ribbon periodically repeated along its main axis. Relaxation shows a minor geometry optimization effect, consisting in a slight reorientation of bonds along the growing direction (see Figure 2).

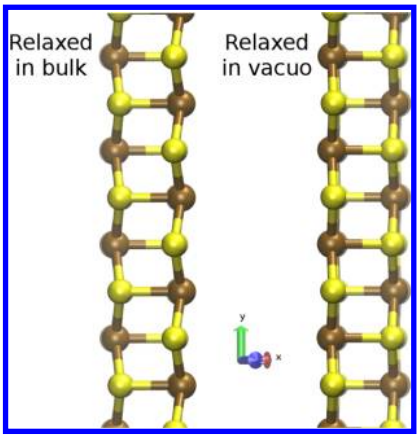

Figure 2. Comparison between the optimized geometry of a Bi_2S_3 ribbon relaxed inside the bulk (left) and a Bi_2S_3 ribbon relaxed in vacuo (right).

A small expansion of about 2% in the (010)-plane is also observed. Consistently with the weak electronic coupling between ribbons found in experiments[7,37] and previous theoretical works,[8,32] our calculations show a small cohesive energy difference between the ribbon and the bulk. In particular, the total energy difference is smaller than ∼0.2 eV/atom to be compared with the large binding energy (2–3 eV/atom) within the atoms of the same ribbon due to the

dx.doi.org/10.1021/jp405740b | J. Phys. Chem. C XXXX, XXX, XXX–XXX

strong Bi−S chemical bonds. Our calculations also show that the bandgap of the single ribbon relaxed in vacuo is 0.1 eV higher than the bandgap of the relaxed Bi_2S_3 bulk (1.6 vs 1.5 eV). This proves that, consistently with the weak electronic coupling between ribbons, there is only a slight dependence of the electronic gap on the size of the system in the (010) plane. This is also consistent with theoretical results[18] for Sb_2S_3. Conversely we will show in the next sections that the electronic confinement is sizable in the direction parallel to the ribbon axis.

Finite Size Nanostructures. We considered Bi_2S_3 single ribbons of variable size within the range 1−10 nm, by properly cutting the infinite ribbon along the (010)-plane. This gives rise to two surfaces and ten dangling bonds for each ribbon-like nanocrystal. First of all, we performed single-point calculations at fixed atomic positions with the PBE exchange-correlation functional. The (010) surfaces give rise to surface states that lie within the fundamental gap. The corresponding HOMO−LUMO gap (HOMO, highest occupied molecular orbital; LUMO, lowest unoccupied molecular orbital) turns out to be as small as 0.3−0.5 eV in all cases. In fact, by inspecting the energy position of the molecular orbitals in Figure 3a and their spatial extension in Figure 4 it is evident that for each ribbon there are ten surface states (six occupied and four unoccupied).

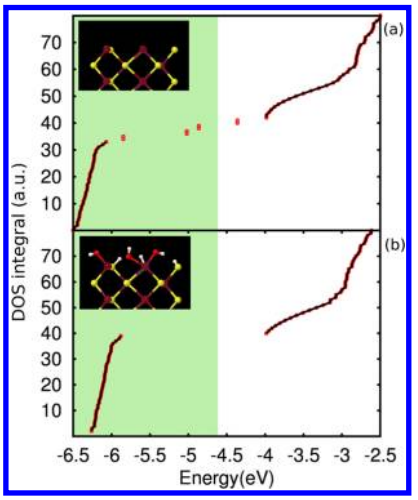

Figure 3. Density of states integral as a function of energy for a 10 nm-long ribbon in its experimental geometry. The green background indicates the filled molecular orbitals. (a) before saturation. The presence of dangling bonds on the surface causes the formations of trap states in between the valence and the conduction band. (b) After saturation. H atoms and OH groups passivate the surface (see inset) and a clean bandgap is obtained.

In particular, the HOMO−LUMO levels correspond to localized surface states that are due to the dangling bonds appearing at the (010) surfaces of the finite ribbon, where the Bi−S bonds are cut. There are two ways of passivating the surface states: by performing structural relaxation of the system through self-healing[31,38] or by suitable saturation of the dangling bonds. In this work, we investigated both methods.

Relaxed Nanocrystals. First, we consider the effect of the relaxation of the atomic positions. In Figure 5a we report the HOMO−LUMO electronic gap of the relaxed Bi_2S_3 nanocrystals as a function of the nanoribbon length. The zero of the energy scale is set to the bandgap of the relaxed infinite ribbon. Let us examine first the part of the curve associated with ribbon

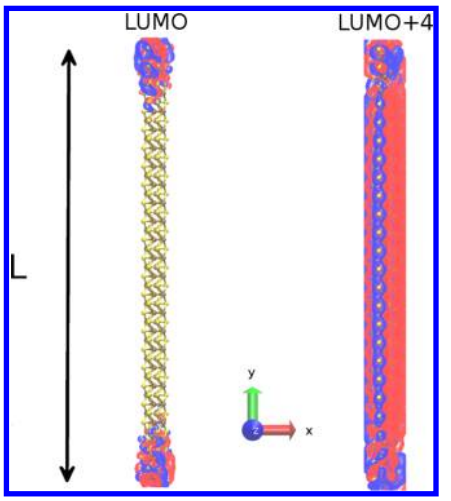

Figure 4. Direct space representation of the molecular orbital isosurfaces for L = 10. Left: The lowest unoccupied molecular orbital (LUMO). The orbital is confined to the ribbon edges: in fact, it is a surface state due to the presence of dangling bonds. Right: The LUMO+4. The orbital is fully delocalized and belongs to the conduction band.

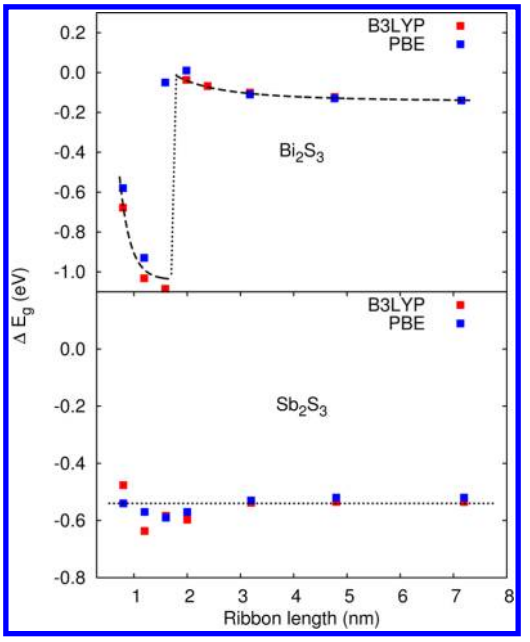

Figure 5. DFT Kohn−Sham gap variation as a function of the ribbon length after relaxation. The zero of the energy scale is set to the PBE bandgap of the relaxed infinite ribbon (1.63 and 1.62 eV for Bi_2S_3 and Sb_2S_3, respectively); the B3LYP and PBE asymptotes have been aligned. (a) Bismuth sufide. An abrupt transition is observed at 2 nm. For long ribbons, the bandgap converges to the value of the periodic case. (b) Antimony sulfide. No transition is observed. The ribbons are unable to self-repair their defects and the bandgap does not converge to the value of the periodic ribbon.

longer than 2 nm. The inverse dependence of the bandgap from the size (*quantum confinement*) is very little: the bandgap converges fast to the asymptotic value with a power law $\propto L^{-2}$ and variations of tens of meV when the length is increased by 1 nm. A more unusual feature is observed when relaxing ribbons shorter than 2 nm where an abrupt lowering of the bandgap by about 1 eV (from 1.6 to 0.7) eV is observed. In order to validate the above behavior we repeated the optimizations by

dx.doi.org/10.1021/jp405740b | J. Phys. Chem. C XXXX, XXX, XXX−XXX

using the B3LYP exchange-correlation functional. Though the B3LYP overestimates the absolute value of the bandgap with respect to PBE, it provides the same bandgap dependence on size and it validates the occurrence of the same jump below 2 nm. In addition, since recent computational results show that the DFT Kohn–Sham gap is sensitive to the inclusion of Bi semicore shell, spin–orbit coupling, and quasi-particle gap correction,[17] we took explicitely into account all the above effects to check the validity of the methodology adopted. In Figure 6, we compare the PBE Kohn–Sham gap dependence

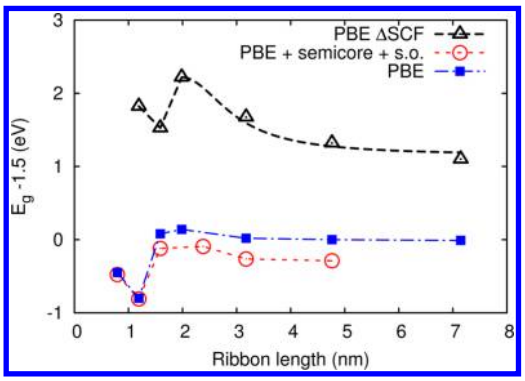

Figure 6. Calculated gap dependence on size according to different corrections to PBE: no corrections (blue); spin–orbit and Bi semicore states (red); quasi-particle correction through the ΔSCF method (black). The lines are guides to the eye. The zero of energy is set to 1.5 eV, i.e., the asymptotic value of the PBE blue curve.

on size with and without spin–orbit and quasi-particle effects. In the case of the spin–orbit correction,[25] we also included the Bi $5s^2 5p^6 5d^{10}$ semicore shell.[26] The quasi-particle gap has been evaluated through the ΔSCF method as difference between the ionization energy and the electron affinity of each cluster.[27] As shown in the picture, the explicit inclusion of all the above effects does not change importantly the functional gap dependence on size. In particular, it is still found a jump and a $\sim L^{-2}$ decay. From a quantitative point of view the combined effect of spin–orbit and semicore is to lower by about ~0.2 eV only the long ribbons energy gap. Conversely, the band gaps of small ribbons are unaffected. In practice, the spin–orbit correction is always about −0.2 eV, while the semicore correction is +0.2 eV for small ribbons and almost zero for long ribbons. A small reduction of the gap discontinuity is therefore calculated by including spin–orbit coupling and semicore electrons with respect to DFT. As for the quasi-particle effects, consistently with the GW result for the bulk material,[17] the ΔSCF gap calculated for finite ribbons is larger than the corresponding DFT gap. However, for finite ribbons, the difference between quasi-particle and DFT gap is considerably larger due to the sizable exciton binding energy expected for finite systems. Overall, we did not find any significant difference as far as the bandgap dependence on size is concerned. The entire discussion on quantum confinement is therefore not affected significantly by the explicit inclusion of spin–orbit, semicore, and quasi-particle effects.

Figure 7 shows separately the variation of the B3LYP HOMO and LUMO energies as a function of the size. The jump of the bandgap at about 2 nm is associated to two corresponding steps in the two curves. The two insets in Figure 7 show the HOMO spatial distribution of a 4-units ribbon (left) or 5-units ribbon (right) around the length of the

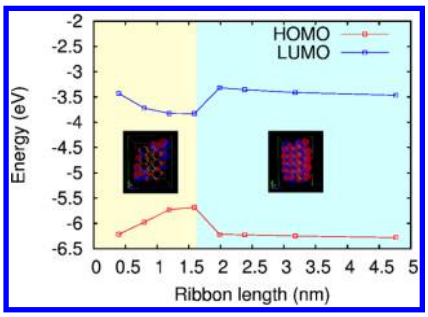

Figure 7. B3LYP HOMO and LUMO energy as a function of the ribbon length. For ribbons shorter then 2 nm, both the MO are localized surface states (left inset). For ribbons longer than 2 nm, relaxation passivates the surfaces, and fully delocalized HOMO and LUMO are observed (right inset).

discontinuity in the electronic gap. The HOMO level of nanoparticles shorter than 2 nm is localized on the edges (left inset). Only for ribbons longer than 2 nm, the HOMO is delocalized on the whole crystal structure (right inset). We conclude that by means of atomic relaxations the ribbons shorter than ~2 nm are unable to get rid of their surface states and still contain localized levels inside the gap. Only for ribbons longer than 2 nm a complete reconstruction of the surfaces is possible providing the disappearance of defect states and restoring a clean gap. It is interesting to compare these observations with a different pnictogen sulfide having the same crystal structure. To this aim we performed similar atomic relaxations on stibnite ribbons using either PBE or B3LYP functionals. As shown in Figure 5b, the bandgap is practically independent of size with no large discontinuities. The asymptotic value of finite nanocrystals is 0.4 eV lower than that of the periodic ribbon. We conclude that Sb_2S_3 is unable to completely self-repair its dangling bonds by surface reconstruction even in the case of 10 nm long ribbons, and the remaining surface states within the gap hinder the occurrence of a clear trend in the bandgap dependence on size.

In order to correlate the above bandgap dependence on size to morphological features, we studied the bond length changes upon relaxation of nanoribbons of different length. In particular, for each nanocrystal we calculated the bismuth–sulfur distance for all atom pairs within the ribbon and calculated the corresponding number distribution (number of bonds as a function of their length). In Figure 8a, we reported a comparison between the Bi–S bond distribution in the relaxed periodic ribbon (red) and the ribbon of length 4 unit cells (green) and 5 unit cells (blue).

These latter systems delimit the discontinuity in the bangap-to-length curve (see Figures 5 and 7). It is clear that the two finite ribbons differ strongly in their Bi–S bond distribution despite their very similar length. We identify two major differences. Going from five to four unit cells, a significant disorder is induced as shown in the larger distribution of lengths found for the 4 units system. Second, a short bond of 2.4 Å is created, which is not present in the ribbons longer than 4 units. Such variations of the ribbon morphology occur only when passing from 4 to 5 units ribbons. The short bond formed for ribbon lengths <2 nm is related to a shortening of the Bi–S bonds involving undercoordinated S atoms at the surfaces. By inspecting the geometrical relaxation of systems of different length, it can be seen that the ribbons longer than 2 nm undergo a particular reconstruction at the surfaces that involves

dx.doi.org/10.1021/jp405740b | J. Phys. Chem. C XXXX, XXX, XXX–XXX

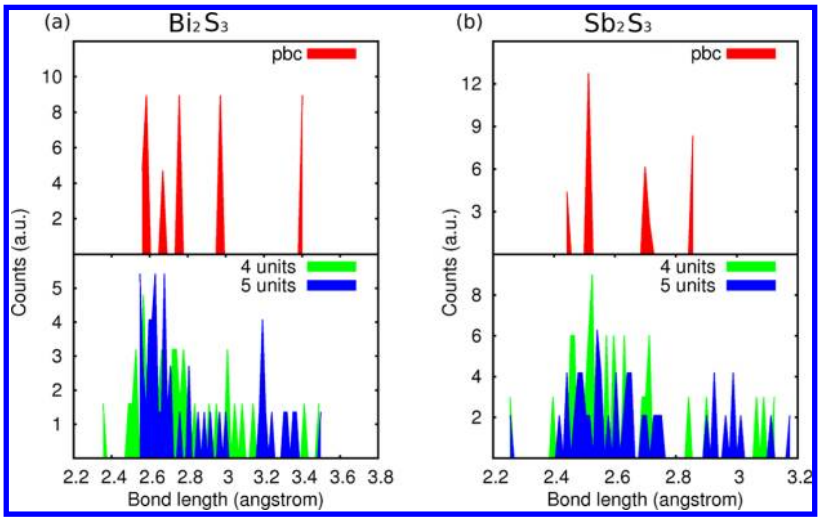

Figure 8. Bond length distribution of standalone ribbons after relaxation. (a) Top: bond distribution for the periodic Bi_2S_3 ribbon. Bottom: bond distribution for ribbons shorter (green) and longer (blue) than the bandgap transition length. The formation of new bonds for long ribbons causes a redistribution of the atomic distances and the disappearance of the short bonds. (b) Bond distribution of Sb_2S_3. In this case, there is no formation of new bonds and the bond distributions of the two finite ribbons are qualitatively similar.

the saturation of the dangling bonds through the formation of new bonds (Figure 9).

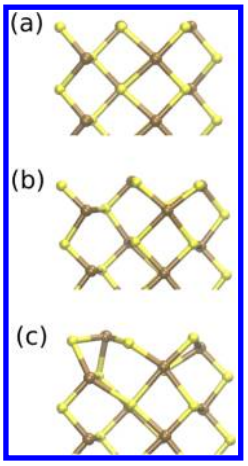

Figure 9. (a) Unrelaxed ribbon (experimental geometry). (b) Relaxation of a ribbon shorter than 2 nm. No new bonds are formed. (c) Relaxation of a ribbon longer than 2 nm. The atoms at the surface recombine to passivate dangling bonds.

Such a reconstruction is not energetically convenient for ribbons shorter than 2 nm. In this case the sulfur atoms at the surface are not able to form new bonds, and their Bi−S bond length is substantially decreased preventing electron sharing with other surface atoms. The results for Bi_2S_3 are quite different from the case of Sb_2S_3 ribbons. In Sb_2S_3 relaxed ribbons there is no surface reconstruction for any size investigated (up to 10 nm) (see Figure 8b), and there is always a short bond of about 2.3 Å in the bond distribution.

We further characterize the ribbon relaxations by calculating the squared effective length $\lambda^2 = \Sigma y_i^2$ along the [010] direction and the relative variation $\Delta_y = ((\lambda^2 - \lambda_0^2)/(\lambda_0^2))^{1/2}$ with respect to the square length of the same nanocrystal at equilibrium (λ_0). The results are reported in Figure 10.

For both Bi_2S_3 and Sb_2S_3, there is a relative y-elongation (tensile strain) of the finite length ribbon with respect to the infinite one. The tensile strain increases for shorter ribbons as expected from the fact that the excess energy density $u = E_S/V$ due to the surfaces is proportional to the surface-to-volume ratio S/V. In fact, $u = E_S/V = 2\gamma S/V \approx (2\gamma)/L$, where γ is the surface energy of the (010)-plane and L is the ribbon length. Consistently with the fact that Sb_2S_3 nanocyrstals do not exhibit a change in surface reconstructions, the elongation turns out to be a monotonically decreasing function of the ribbon length. At variance, in the case of Bi_2S_3, we find a step at 2 nm in the strain function that corresponds to the different surface reconstructions discussed above.

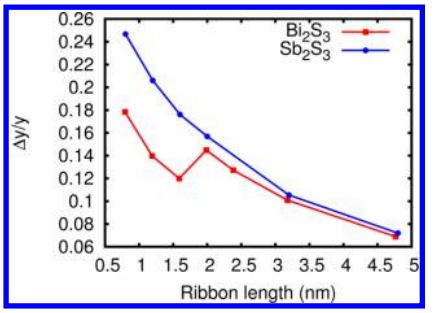

Figure 10. Relative elongation of the ribbons as a function of their length. Sb_2S_3 shows a smooth trend, where the elongation monotonically decreases with increasing length. However, Bi_2S_3 presents a step occurring exactly at the bandgap transition length.

Overall, the above analysis shows that the fine interplay between the strain and surface reconstruction induces a nonmonotonic dependence of the HOMO−LUMO gap of the relaxed Bi_2S_3 ribbons. This makes difficult to recognize the occurrence of quantum confinement. In order to disentangle the role of atomic relaxations and surface effects from quantum confinement, we performed an additional analysis by accurately saturating unrelaxed nanostructures.

Saturated Nanocrystals. A second set of Bi_2S_3 nanoparticles (hereafter referred to as unrelaxed) is obtained by removing the surface states by chemical saturation of the dangling bonds while keeping ribbons in their perfect crystal geometry at experimental lattice size. We saturated undercoordinated sulfur and bismuth atoms on the ribbon edges by H and OH groups,

dx.doi.org/10.1021/jp405740b | J. Phys. Chem. C XXXX, XXX, XXX−XXX

respectively (see inset in Figure 3b). We performed a local relaxation where only saturating atoms are allowed to move. The resulting electronic structure gives a clean bandgap with no surface states occurring in the ribbons (Figure 3b). The change of the bandgap as a function of the ribbon length (ΔE_g) is reported in Figure 11a, in which both the PBE and B3LYP results are present. The zero of the energy scale corresponds to the unrelaxed infinite ribbon gap.

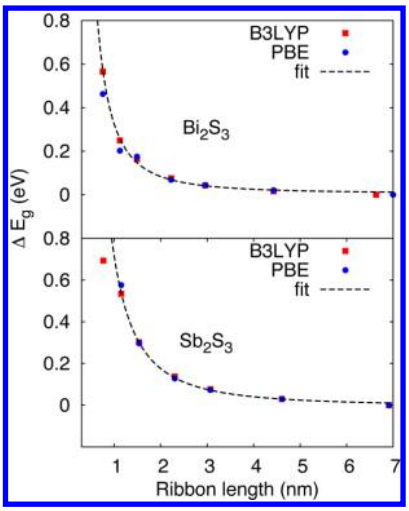

Figure 11. Quantum confinement energies of saturated ribbons as a function of their length calculated by PBE (circles) and B3LYP (squares) functionals for Bi_2S_3 (top panel) and Sb_2S_3 (bottom panel). Dashed lines correspond to numerical fit (see text).

As one can see, there is a monotonic increase of the bandgap with decreasing size consistent with a sizable quantum confinement of electrons in the system. This behavior can be nicely reproduced by a power law function of the ribbon length $f(L) \propto 1/L^2$. We emphasize that L^{-2} is the standard quantum confinement law. Figure 11a reveals that it is possible to significantly tune the bandgap only for nanocrystals smaller than ~3 nm: for larger systems, quantum confinement is hardly detectable. For long unrelaxed Bi_2S_3 ribbons, the bandgap converges to the value of the infinite ribbon calculated by using the QUANTUM ESPRESSO code. It should be noticed that the overall electronic confinement attainable by reducing the ribbon length is around 0.6 eV for both PBE and B3LYP, much higher than the quantum effect observed when passing from the bulk to the infinite ribbon (0.1−0.2 eV). We conclude that the electronic coupling between neighbor ribbons plays only a secondary role in the delocalization of the electrons: the confinement is primarily due to the length of the ribbons.

The above analysis has been repeated for the case of Sb_2S_3 unrelaxed ribbons as well. The results are reported in Figure 11b, and the bandgap has the same L^{-2} asymptotic behavior as that in the Bi_2S_3 case. In both cases, sizable variation of the bandgap is expected only for nanostructures smaller than about 3 nm.

Since the optical gap observed experimentally concerns an excited state of the system, we used TDDFT to perform the same analysis on quantum confinement discussed above. The calculated optical gap of the nanocrystals depends on size consistently with the previous analysis. The asymptotic bandgap is 1.5 eV and the quantum confinement is weak for nanocrystals longer then 3 nm. Hence, we can conclude that bismuth sulfide allows large tunability only if the nanoparticles are smaller than 3 nm.

CONCLUSIONS

In the present study we focused on the morphology and optoelectronic properties of Bi_2S_3 nanocrystals. Choosing the ribbon as the building block for our nanostructures, we explored the effects of both relaxation and saturation of finite size systems. For relaxed nanocrystals, the quantum confinement effect is hidden by the persistence of defects on the ribbon edges. In particular, only the ribbons longer than 2 nm are able to reconstruct their surface in order to efficiently passivate electronic trap states. For all lengths, a tensile strain of the ribbon with respect to the periodic system is observed. In addition we studied the quantum confinement by keeping the nanocrystals in their experimental geometry and saturating the dangling bonds by means of hydrogen atoms and OH groups. The dependence of the bandgap as a function of the ribbon length L was found to be a power law $\propto L^{-\alpha}$ with $\alpha = 2$. The DFT calculations were performed with two different functionals (PBE and B3LYP), and in all cases, the trends we found are in very good agreement. With the PBE functional we estimate a bandgap of 1.6 eV for long ribbons, that lies in between the experimental range reported in literature (1.2−1.7 eV).[33−36] Such bandgap ideally increases up to 2.2 eV for nanostructures of length ~1 nm. We studied also the isostructural material Sb_2S_3 in comparison with Bi_2S_3. We concluded that bismuth sulfide shows a better capability to reconstruct its surfaces with respect to stibnite. Overall the above results suggest that, from the theoretical point of view, the environmental friendly bismuthinite is a valid alternative to the toxic stibnite, as far as concerns of confinement, optical and electronic properties.

AUTHOR INFORMATION

Corresponding Authors

*(V.C.) E-mail: vasco.calzia@dsf.unica.it.

*(A.M.) E-mail: mattoni@iom.cnr.it. Phone: +39 070 6754868. Fax: +39 070 6754892.

Notes

The authors declare no competing financial interest.

ACKNOWLEDGMENTS

We acknowledge A. Filippetti (CNR-IOM Cagliari), A. Musinu (Dept. of Chemistry, University of Cagliari), and M. Saba (Dept. of Physics, University of Cagliari) for useful discussions. This work has been funded by the Italian Institute of Technology under Project Seed "POLYPHEMO" and IIT "Platform Computation", by Regione Autonoma della Sardegna under L. R. 7/2007 CRP-18013 "Nanocristalli per la produzione di idrogeno dall'energia" and CRP-249078 "Nanomateriali eco-compatibili per celle fotovoltaiche a stato solido di nuova generazione", by MIUR under PON 2007-2013 (Project NETERGIT), and by Consiglio Nazionale delle Ricerche (Progetto Premialità RADIUS). We acknowledge computational support by CINECA through ISCRA Initiative (Project OPTO-BIS).

REFERENCES

(1) Lai, C.-H.; Lu, M.-Y.; Chen, L.-J. Metal Sulfide Nanostructures: Synthesis, Properties and Applications in Energy Conversion and Storage. *J. Mater. Chem.* **2012**, *22*, 19−30.

(2) Wu, Y.; Wadia, C.; Ma, W.; Sadtler, B.; Alivisatos, A. P. Synthesis and Photovoltaic Application of Copper(I) Sulfide Nanocrystals. *Nano Lett.* **2008**, *8*, 2551−2555.
(3) Li, T.-L.; Lee, Y.-L.; Teng, H. $CuInS_2$ Quantum Dots Coated with CdS as High-Performance Sensitizers for TiO_2 Electrodes in Photoelectrochemical Cells. *J. Mater. Chem.* **2011**, *21*, 5089−5098.
(4) Bierman, M. J.; Jin, S. Potential Applications of Hierarchical Branching Nanowires in Solar Energy Conversion. *Energy Environ. Sci.* **2009**, *2*, 1050−1059.
(5) Chang, J. A.; Rhee, J. H.; Im, S. H.; Lee, Y. H.; Kim, H.-J.; Seok, S. I.; Nazeeruddin, M. K.; Grätzel, M. High-Performance Nanostructured Inorganic−Organic Heterojunction Solar Cells. *Nano Lett.* **2010**, *10*, 2609−2612.
(6) Mohan, R. Green Bismuth. *Nat. Chem.* **2010**, *2*, 336−336.
(7) Lundegaard, L.; Makovicky, E.; Boffa-Ballaran, T.; Balic-Zunic, T. Crystal Structure and Cation Lone Electron Pair Activity of Bi_2S_3 between 0 and 10 GPa. *Phys. Chem. Miner.* **2005**, *32*, 578−584.
(8) Caracas, R.; Gonze, X. First-Principles Study of the Electronic Properties of A_2B_3 Minerals, with A = Bi,Sb and B = S,Se. *Phys. Chem. Miner.* **2005**, *32*, 295−300.
(9) Konstantatos, G.; Levina, L.; Tang, J.; Sargent, E. H. Sensitive Solution-Processed Bi_2S_3 Nanocrystalline Photodetectors. *Nano Lett.* **2008**, *8*, 4002−4006.
(10) Rath, A. K.; Bernechea, M.; Martinez, L.; de Arquer, F. P. G.; Osmond, J.; Konstantatos, G. Solution-Processed Inorganic Bulk Nano-Heterojunctions and Their Application to Solar Cells. *Nat. Photon.* **2012**, *6*, 529−534.
(11) Murray, C.; Sun, S.; Gaschler, W.; Doyle, H.; Betley, T. A.; Kagan, C. Colloidal Synthesis of Nanocrystals and Nanocrystal Superlattices. *IBM J. Res. Dev.* **2001**, *45*, 47−56.
(12) Li, H.; Chen, D.; Li, L.; Tang, F.; Zhang, L.; Ren, J. Size- and Shape-Controlled Synthesis of PbSe and PbS Nanocrystals via a Facile Method. *CrystEngComm* **2010**, *12*, 1127−1133.
(13) Rath, A. K.; Bernechea, M.; Martinez, L.; Konstantatos, G. Solution-Processed Heterojunction Solar Cells Based on p-Type PbS Quantum Dots and n-Type Bi_2S_3 Nanocrystals. *Adv. Mater.* **2011**, *23*, 3712−3717.
(14) Pattantyus-Abraham, A. G.; Kramer, I. J.; Barkhouse, A. R.; Wang, X.; Konstantatos, G.; Debnath, R.; Levina, L.; Raabe, I.; Nazeeruddin, M. K.; Grätzel, M.; Sargent, E. H. Depleted-Heterojunction Colloidal Quantum Dot Solar Cells. *ACS Nano* **2010**, *4*, 3374−3380.
(15) Larson, P.; Greanya, V. A.; Tonjes, W. C.; Liu, R.; Mahanti, S. D.; Olson, C. G. Electronic Structure of Bi_2X_3 (X = S,Se,T) Compounds: Comparison of Theoretical Calculations with Photoemission Studies. *Phys. Rev. B* **2002**, *65*, 085108.
(16) Patrick, C. E.; Giustino, F. Structural and Electronic Properties of Semiconductor-Sensitized Solar-Cell Interfaces. *Adv. Funct. Mater.* **2011**, *21*, 4663−4667.
(17) Filip, M. R.; Patrick, C. E.; Giustino, F. *GW* Quasiparticle Band Structures of Stibnite, Antimonselite, Bismuthinite, and Guanajuatite. *Phys. Rev. B* **2013**, *87*, 205125.
(18) Vadapoo, R.; Krishnan, S.; Yilmaz, H.; Marin, C. Self-Standing Nanoribbons of Antimony Selenide and Antimony Sulfide with Well-Defined Size and Band Gap. *Nanotechnology* **2011**, *22*, 175705.
(19) Kohn, W.; Sham, L. J. Self-Consistent Equations Including Exchange and Correlation Effects. *Phys. Rev.* **1965**, *140*, A1133−A1138.
(20) Giannozzi, P.; Baroni, S.; Bonini, N.; Calandra, M.; Car, R.; Cavazzoni, C.; Ceresoli, D.; Chiarotti, G. L.; Cococcioni, M.; Dabo, I.; Dal Corso, A.; de Gironcoli, S.; Fabris, S.; Fratesi, G.; Gebauer, R.; Gerstmann, U.; Gougoussis, C.; Kokalj, A.; Lazzeri, M.; Martin-Samos, L.; Marzari, N.; Mauri, F.; Mazzarello, R.; Paolini, S.; Pasquarello, A.; Paulatto, L.; Sbraccia, C.; Scandolo, S.; Sclauzero, G.; Seitsonen, A. P.; Smogunov, A.; Umari, P.; Wentzcovitch, R. M. QUANTUM ESPRESSO: a Modular and Open-Source Software Project for Quantum Simulations of Materials. *J. Phys.: Condens. Matter* **2009**, *21*, 395502.
(21) Perdew, J. P.; Burke, K.; Ernzerhof, M. Generalized Gradient Approximation Made Simple. *Phys. Rev. Lett.* **1996**, *77*, 3865−3868.
(22) Troullier, N.; Martins, J. L. Efficient Pseudopotentials for Plane-Wave Calculations. *Phys. Rev. B* **1991**, *43*, 1993−2006.
(23) *TURBOMOLE*, V6.4, 2012; available from http://www.turbomole.com.
(24) Becke, A. D. Density Functional Thermochemistry. III. The Role of Exact Exchange. *J. Chem. Phys.* **1993**, *98*, 5648−5652.
(25) Armbruster, M. K.; Weigend, F.; van Wullen, C.; Klopper, W. Self-Consistent Treatment of Spin−Orbit Interactions with Efficient Hartree−Fock and Density Functional Methods. *Phys. Chem. Chem. Phys.* **2008**, *10*, 1748−1756.
(26) Metz, B.; Stoll, H.; Dolg, M. Small-Core Multiconfiguration-Dirac−Hartree−Fock-adjusted Pseudopotentials for Post-d Main Group Elements: Application to PbH and PbO. *J. Chem. Phys.* **2000**, *113*, 2563−2569.
(27) Jones, R. O.; Gunnarsson, O. The Density Functional Formalism, Its Applications and Prospects. *Rev. Mod. Phys.* **1989**, *61*, 689−746.
(28) Runge, E.; Gross, E. K. U. Density-Functional Theory for Time-Dependent Systems. *Phys. Rev. Lett.* **1984**, *52*, 997−1000.
(29) Casida, M. E. In *Recent Advances in Density Functional Theory*; Chong, D. P., Ed.; World Scientific: Singapore, 1995; Vol. *I*.
(30) Caddeo, C.; Malloci, G.; De Angelis, F.; Colombo, L.; Mattoni, A. Optoelectronic Properties of $(ZnO)_{60}$ Isomers. *Phys. Chem. Chem. Phys.* **2012**, *14*, 14293−14298.
(31) Malloci, G.; Chiodo, L.; Rubio, A.; Mattoni, A. Structural and Optoelectronic Properties of Unsaturated ZnO and ZnS Nanoclusters. *J. Phys. Chem. C* **2012**, *116*, 8741−8746.
(32) Sharma, Y.; Srivastava, P.; Dashora, A.; Vadkhiya, L.; Bhayani, M.; Jain, R.; Jani, A.; Ahuja, B. Electronic Structure, Optical Properties and Compton Profiles of Bi_2S_3 and Bi_2Se_3. *Solid State Sci.* **2012**, *14*, 241−249.
(33) Yesugade, N.; Lokhande, C.; Bhosale, C. Structural and Optical Properties of Electrodeposited Bi_2S_3, Sb_2S_3 and As_2S_3 Thin Films. *Thin Solid Films* **1995**, *263*, 145−149.
(34) Lukose, J.; Pradeep, B. Electrical and Optical Properties of Bismuth Sulphide [Bi_2S_3] Thin Films Prepared by Reactive Evaporation. *Solid State Commun.* **1991**, *78*, 535−538.
(35) Chen, B.; Uher, C.; Iordanidis, L.; Kanatzidis, M. G. Transport Properties of Bi_2S_3 and the Ternary Bismuth Sulfides $KBi_{6.33}S_{10}$ and $K_2Bi_8S_{13}$. *Chem. Mater.* **1997**, *9*, 1655−1658.
(36) Mizoguchi, H.; Hosono, H.; Ueda, N.; Kawazoe, H. Preparation and Electrical Properties of Bi_2S_3 Whiskers. *J. Appl. Phys.* **1995**, *78*, 1376−1378.
(37) Lundegaard, L. F.; Miletich, R.; Balic-Zunic, T.; Makovicky, E. Equation of State and Crystal Structure of Sb_2S_3 between 0 and 10 GPa. *Phys. Chem. Miner.* **2003**, *30*, 463−468.
(38) Grätzel, M.; Janssen, R. A. J.; Mitzi, D. B.; Sargent, E. H. Materials Interface Engineering for Solution-Processed Photovoltaics. *Nature* **2012**, *488*, 304−312.